Bol. Soc. Paran. Mat.
©SPM – E-ISSN-2175-1188
SPM: www.spm.uem.br/bspm

(3s.) **v. 2026 (44)** : 1–17.
ISSN-0037-8712
doi:10.5269/bspm.79800

Modelling and Simulation of Chemically Reactive Micropolar Nanofluid Flow with Viscous Dissipation and Suction in a Porous Medium

Sreedhar Sarma Gobburu

ABSTRACT: The objective of the present analysis is to investigate the heat and mass transfer characteristics of a micropolar nanofluid flow driven by a permeable surface with suction effects, incorporating the influence of viscous dissipation and chemical reaction. The thermal behavior is further enhanced by including radiative heat transfer and Dufour diffusion mechanisms. The governing nonlinear partial differential equations accounting for momentum, microrotation, energy, and concentration are transformed into a dimensionless form using similarity transformations. The resulting system of coupled ordinary differential equations is solved using MATLAB's robust bvp5c solver. Validation of the numerical approach is carried out through comparison with published results in the limiting cases. Parametric impacts on velocity, microrotation, temperature, and concentration profiles are thoroughly analyzed. The results reveal that viscous dissipation amplifies thermal gradients while chemical reactions suppress concentration levels. Additionally, variations in surface quantities such as skin friction, local Nusselt number, and local Sherwood number are evaluated to assess boundary layer behavior. The extended model offers a more comprehensive understanding of thermally and chemically active micropolar nanofluid flows, with implications in thermal processing, energy systems, and biomedical engineering.

Keywords: Micropolar nanofluid, porous medium, viscous dissipation, magnetohydrodynamics.

Contents

1. Introduction

The study of micropolar nanofluids has garnered significant attention due to their distinctive microstructure, which includes microrotation effects and non-Newtonian behavior, making them suitable for applications in lubrication, polymer processing, and biomedical systems. The foundational work of Eringen [1] introduced the theory of micropolar fluids, laying the groundwork for later advancements in micro structured fluid dynamics. The development of nanofluid technology, as pioneered by Choi and Eastman [2], significantly improved the thermal conductivity of base fluids by dispersing nanoparticles, further extended by Buongiorno [3], who introduced a two-component nanofluid model incorporating Brownian motion and thermophoresis.

Micropolar nanofluids, which merge the effects of nanoparticle dispersion and microrotation, exhibit complex behavior under various physical influences. Muhaimin *et al.* [4] and Shateyi [5] analyzed the effect of thermal radiation and chemical reaction on heat and mass transfer under suction conditions, highlighting the role of radiative and reactive transport in engineering flows. The investigation by Khan and Pop [6] offered baseline insights into nanofluid boundary layer flow, while further exploration by Narender *et al.* [7] and Govardhan *et al.* [8] examined the influence of viscous dissipation and chemical reaction in Casson nanofluid flows.

The introduction of variable heat flux and micropolar behavior in thermal analysis was presented by Ishak *et al.* [9], and subsequent work by Srinivasacharya and Jagadeeshwar [10] studied the effects of

2020 *Mathematics Subject Classification:* 76S05, 76A05, 76D05, 76R05, 76W05.
Submitted October 29, 2025. Published March 19, 2026

thermal conductivity variation and internal heat generation. Hydromagnetic effects on micropolar flows were investigated by Bég *et al.* [11], and recent work by Ajala and Adegbite [12] incorporated radiation and chemical reactions in micropolar nanofluid dynamics. Sachhin *et al.* [13] extended the model to include inclined magnetic fields and entropy generation.

The combined impacts of thermal radiation, Brownian motion, and thermophoresis were studied by Sulochana and Mahalaxmi [14], while the 3D extension of Casson nanofluid flow with rotating frames was modelled by Gobburu *et al.* [15]. Khan *et al.* [16] provided insight into buoyancy-driven micropolar nanofluid flows with dissipation, and Panda *et al.* [17] explored slip effects in radiating micropolar fluids. Alqahtani *et al.* [18] and Zegeye *et al.* [19] presented novel configurations involving porous media and Joule heating. Heat and mass transfer analysis of mixed convection flow over a stretching surface filled with a viscoelastic fluid was studied by Hayat *et al.* [20]. Rehman *et al.* [21] investigated transient behaviours in hybrid nanofluids under viscous dissipation, and Ghosh and Mukhopadhyay [22] included thermal radiation and nanoparticle flux conditions. Sarma *et al.* [23] presented a comprehensive model incorporating heat source/sink and inclined porous stretching implications. Muhammad *et al.* [24] investigated the bio-convective characteristics of reactive micropolar nanofluids.

The current study is further motivated by the recent work of Abbas *et al.* [25], which analyzed micropolar nanofluid suction effects in rotating geometries. Additionally, Abdelgaber *et al.* [26], Srilatha *et al.* [27], and Zigta [28] contributed to the understanding of thermal and reactive behavior in micropolar flows. Adeyemi *et al.* [29] and Meenakshi *et al.* [30] emphasized radiation and generation/absorption dynamics, while Ahmed and Al-Radaideh [31] integrated nonlinear heat generation in Williamson micropolar fluids. Lastly, Shehzad *et al.* [32] examined MHD squeezing flows with advanced thermal relaxation models.

These works collectively emphasize the need for an extended model that integrates viscous dissipation, chemical reaction, suction, and radiation effects in micropolar nanofluid flows. This study thus aims to provide a comprehensive theoretical and numerical framework using similarity transformations and MATLAB's bvp5c solver to evaluate heat and mass transport behaviours under porous boundary conditions. The analysis is validated through existing literature and presents new insights applicable to engineering systems in heat transfer, cooling technologies, and bioengineering applications.

2. Mathematical Formulation

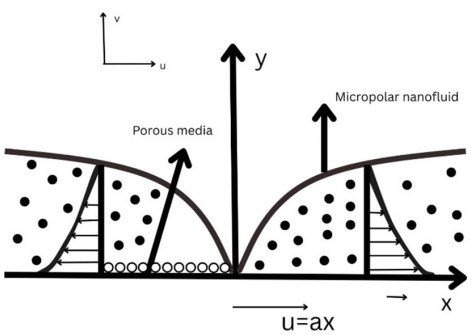

Figure 1: Flow model

The present investigation focuses on the heat and mass transfer characteristics of a steady, two-dimensional flow of an electrically conducting micropolar nanofluid induced by a porous, linearly stretching sheet. The flow is assumed to occur within a saturated porous medium, where mass suction effects are incorporated to represent permeability influences. A Cartesian coordinate system is employed to construct the governing equations, as illustrated schematically in Figure 1. The energy equation is extended to include thermal radiation and the Dufour effect, capturing additional heat transfer mechanisms. The flow regime is assumed to be laminar with a low Reynolds number, ensuring that the boundary layer approximations are valid. To accurately model nanoparticle behavior, the Buongiorno two-phase nanofluid

model is adopted, which accounts for both Brownian motion and thermophoretic diffusion. In the coordinate system, the velocity components are defined such that u represents the velocity along the surface and v denotes the transverse component normal to the surface. The microrotation of microelements is represented by N. Boundary conditions are defined by T_w for surface temperature, T_∞ for ambient fluid temperature, C_w for surface concentration, and C_∞ for free-stream concentration, while C and T denote the local nanoparticle concentration and temperature within the boundary layer, respectively.
The modelled equations that adhere to these constraints are:

$$\frac{\partial u}{\partial x}+\frac{\partial v}{\partial y}=0 \tag{2.1}$$

$$u\frac{\partial u}{\partial x}+v\frac{\partial v}{\partial y}=\left(\nu+\frac{k}{\rho}\right)\frac{\partial^2 u}{\partial y^2}+\frac{k}{\rho}\frac{\partial N}{\partial y}-\left(\frac{\sigma B_0^2}{\rho}+\frac{\mu\varphi_1}{k}\right)u \tag{2.2}$$

$$u\frac{\partial N}{\partial x}+v\frac{\partial N}{\partial y}=\frac{1}{\rho_j}\left[r\frac{\partial^2 N}{\partial y^2}-k\left(2N+\frac{\partial u}{\partial y}\right)\right] \tag{2.3}$$

$$u\frac{\partial T}{\partial x}+v\frac{\partial T}{\partial y}=\left(\alpha+\frac{16\sigma^* T_\infty^3}{3k^*\rho c_p}\right)\frac{\partial^2 T}{\partial y^2}+\tau_w\left[D_B\frac{\partial C}{\partial y}\frac{\partial T}{\partial y}+\frac{D_T}{T_\infty}\left(\frac{\partial T}{\partial y}\right)^2\right]+\frac{D_T}{C_s}\frac{K_T}{C_p}\frac{\partial^2 C}{\partial y^2}+\frac{\mu}{\rho c_p}\left(\frac{\partial u}{\partial y}\right)^2 \tag{2.4}$$

$$u\frac{\partial C}{\partial x}+v\frac{\partial C}{\partial y}=D_B\frac{\partial^2 C}{\partial y^2}+\frac{D_T}{T_\infty}\frac{\partial^2 T}{\partial y^2}-k_r(C-C_\infty) \tag{2.5}$$

The boundary conditions are as follows

$$\begin{aligned} &v=0,\ \ u=U_w=ax,\ v=-v_w,\ N=-m\frac{\partial u}{\partial y},\ T=T_w,\ C=C_w \text{ at } \ y=0\\ &u\to 0,\ N\to 0,\ T\to T_0,\ C\to C_\infty \text{ as } \ y\to\infty \end{aligned} \tag{2.6}$$

By applying the similarity transformations listed below,

$$\begin{aligned} &\eta=y\sqrt{\frac{a}{\vartheta}},\ u=axf'(\eta),\ v=-\sqrt{a\vartheta}\ f(\eta),\ N=\sqrt{\frac{a}{\vartheta}}axg(\eta),\\ &\theta(\eta)=\frac{T-T_\infty}{T_w-T_\infty},\ \phi(\eta)=\frac{C-C_\infty}{C_w-C_\infty} \end{aligned} \tag{2.7}$$

The following equations are derived from the governing equations (2.2) to (2.5)

$$(1+K)f'''+Kg'-f'^2+ff''-(M+\in)f'=0 \tag{2.8}$$

$$\left(1+\frac{K}{2}\right)g''-2Kg-Kf''-f'g+fg'=0 \tag{2.9}$$

$$\frac{1}{\Pr}\left(1+\frac{4}{3}Rd\right)\theta''+Nb\phi'\theta'+Nt(\theta')^2+f\theta'+D_f\phi''+Ec(f'')^2=0 \tag{2.10}$$

$$\frac{1}{Sc}\phi''+f\phi'+\frac{1}{Sc}\frac{Nt}{Nb}\theta''-\gamma\phi=0 \tag{2.11}$$

With

$$\begin{aligned} &f(0)=Vc,\ f'(0)=d,\ g(0)=-mf''(0),\ \theta(0)=1,\ \phi(0)=1,\\ &f(\eta)\to 0,\ g(\eta)\to 0,\ \theta(\eta)\to 0,\ \phi(\eta)\to 0,\ \eta\to\infty \end{aligned} \tag{2.12}$$

with micropolar parameter $K=\frac{k}{\rho}$, thermophoresis parameter $Nt=\frac{\tau_w D_B(T_w-T_\infty)}{T_\infty\nu}$, porosity parameter $\in=\frac{\mu\varphi_1}{ka}$, Magnetic parameter $M=\frac{\sigma B_0^2}{\rho a}$, Brownian parameter $Nb=\frac{\tau_w D_B(C_w-C_\infty)}{\nu}$, Radiation number $Rd=\frac{16\sigma^* T_\infty^3}{3kk^*}$, Suction parameter $Vc=\frac{v_w}{\sqrt{a\vartheta}}$, Schmidt number $Sc=\frac{\nu}{D_B}$, Prandtl number $\Pr=\frac{\nu}{\alpha}$, Eckert number $Ec=\frac{a^2}{c_p(T_w-T_\infty)}$, Chemical reaction parameter $\gamma=\frac{k_r}{a}$.

Skin friction coefficient C_f, local Nusselt number Nu_x and local Sherwood number Sh_x are the physical quantities of importance. They are defined as $C_f = \frac{\tau_w}{\rho U_w^2}$, $Nu_x = \frac{xq_w}{k(T_w - T_\infty)}$, $Sh_x = \frac{xj_w}{D_T(C_w - C_\infty)}$ where τ_w, q_w and j_w are the wall skin friction, the wall heat flux and the mass flux. In terms of dimensionless form, we have $C_f\sqrt{Re_x} = f''(0)$, $Nu_x Re_x^{\frac{-1}{2}} = -\theta'(0)$, $Sh_x Re_x^{\frac{-1}{2}} = -\phi'(0)$ where $Re_x = \frac{U_w x}{\nu}$ is the local Reynolds number.

3. Numerical Solution

The governing boundary layer equations are obtained by applying suitable similarity transformations to the original partial differential equations that describe mass, momentum, microrotation, energy, and concentration transport. These equations comprise a coupled system of nonlinear ordinary differential equations (2.8) to (2.11) subject to the boundary conditions (2.12). These ODEs, subject to nonlinear and coupled boundary conditions, do not admit analytical solutions and thus require a robust numerical treatment.

In this research, the boundary value problem is solved using MATLAB's built-in bvp5c solver, which implements a fifth-order accurate collocation method based on the Lobatto IIIa formula. The solver is particularly well-suited for stiff or moderately stiff problems and provides an adaptive mesh refinement capability for enhanced solution accuracy. Using similarity variables, the system of equations is first transformed into a set of nine first-order ordinary differential equations.

$$\begin{aligned} &y_1 = f,\ y_2 = f',\ y_3 = f'', \\ &y_4 = g,\ y_5 = g', \\ &y_6 = \theta,\ y_7 = \theta', \\ &y_8 = \phi,\ y_9 = \phi' \end{aligned} \tag{3.1}$$

Substituting these into the governing equations yields the following first-order system:

$$y_1' = y_2, \tag{3.2}$$

$$y_2' = y_3,$$

$$y_3' = \frac{1}{1+K}\left({y_2}^2 - y_1 y_3 + (M + \in) y_2 - K y_5\right), \tag{3.3}$$

$$y_4' = y_5,$$

$$y_5' = \frac{1}{1+\frac{K}{2}}\left(2K y_4 + K y_3 + y_2 y_4 - K y_1 y_5\right), \tag{3.4}$$

$$y_6' = y_7,$$

$$y_7' = \frac{1}{\left(\frac{1+\frac{4}{3}Rd}{\Pr}\right)}\left(-Nb y_9 y_7 - Nt {y_7}^2 - Ec {y_3}^2 - y_1 y_7 - Df y_9\right), \tag{3.5}$$

$$y_8' = y_9,$$

$$y_9' = -Sc y_1 y_9 - \frac{Nt}{Nb} y_7' + \gamma y_8 \tag{3.6}$$

Where the corresponding B. Cs are

$$\begin{aligned} &y_1(0) = Vc,\ y_2(0) = d,\ y_4(0) = -m y_3(0),\ y_6(0) = 1,\ y_8(0) = 1, \\ &y_1(\eta) \to 0,\ y_4(\eta) \to 0,\ y_6(\eta) \to 0,\ y_8(\eta) \to 0,\ \eta \to \infty \end{aligned} \tag{3.7}$$

Convert the system to first-order ODE's as above. We define an initial mesh over $\eta \in [0,\ \eta_\infty]$ by taking $\eta_\infty = 10$ then we provide an initial guess for all dependent variables. Implement the boundary conditions as a separate function by calling bvp5c (@odefun, @bcfun, solinit) in MATLAB to compute the solution.

4. Results and Discussion

The nonlinear ODEs (2.8) to (2.11) subject to the boundary conditions (2.12) were solved using MATLAB's bvp5c solver. The impact of different parameters like Micropolar fluid parameter, Suction parameter, Radiation number, Eckert number, Brownian motion parameter, Thermophoresis parameter, Prandtl number, Chemical reaction parameter, Skin friction coefficient, local Nusselt number and local Sherwood number are calculated numerically and plotted on different profiles f', g, θ and ϕ in Figures 2- 19. To confirm the correctness of the current finding, the calculated $f''(0)$ values were compared to those published by Hayat *et al.* [20] and Abbas *et al.* [25], as shown in Table 1, which showed extremely excellent agreement. Table 2. displays the values of skin friction coefficient, local Nusselt number and local Sherwood number for various non-dimensional parameters. The magnitude of skin friction coefficient rises with increasing values of M and $\in$, but decreases with higher values of K. We observed that increasing Rd increases the magnitude of the local Nusselt number, whereas increasing Nb,Nt, Ec and γ decreases it. The magnitude of local Sherwood number grows as Rd, Nb, Ec and γ increase, but decreases as Nt increases.

Table 1: Variation of $f''(0)$ when $K = M = Vc = m = Ec = \gamma = 0$ for different values of porous parameter $\in$

$\in$	Hayat *et al.* [20]	Abbas *et al.* [25]	Present results
0	-1.000000	-1.000000	-1.001216
0.5	-1.224747	-1.224746	-1.224884
1	-1.414217	-1.414215	-1.414235
1.5	-1.581147	-1.581145	-1.581143
2	-1.732057	-1.732058	-1.732052

The impact of Micropolar fluid parameter is depicted in Figures 2-5. An increase in the micropolar parameter K causes a decrease in the axial velocity $f'(\eta)$, as part of the momentum is absorbed by the rotational motion of the microelements. Simultaneously, the microrotation $g(\eta)$ becomes more prominent, indicating stronger rotational effects due to the microstructure of the fluid which is observed in Figure 2-3. The temperature profile $\theta(\eta)$ in Fig 4 shows a slight enhancement with increasing K, as microrotation tends to introduce additional internal friction and thus more thermal energy. The concentration profile is also mildly increased in Figure 5, potentially due to reduced axial transport and stronger coupling between microrotation and species diffusion.

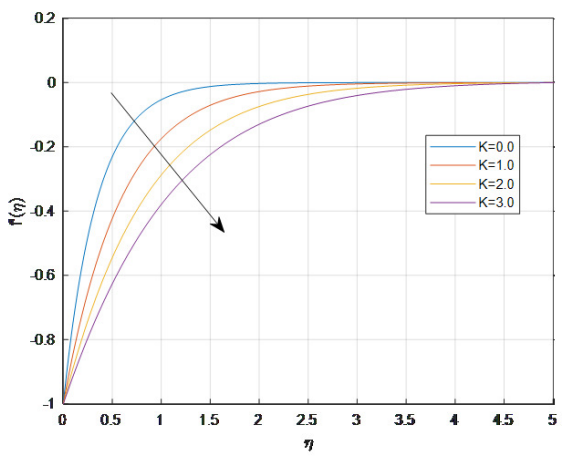

Figure 2: Change in velocity profile f' with varying K

Table 2: Variation of Skin friction $f''(0)$, local Nusselt number $-\theta'(0)$ and local Sherwood number $-\phi'(0)$ for various parameters

K	M	$\in$	Pr	Rd	Nb	Nt	Ec	γ	$f''(0)$	$-\theta'(0)$	$-\phi'(0)$
0.0	0.5	0.3	1	0.2	0.2	0.5	0.5	0.5	3.302776	-0.285646	3.700703
1.0									2.036809	0.409631	2.954098
2.0									1.500127	0.684033	2.644810
1	0.0	0.3	1	0.2	0.2	0.5	0.5	0.5	1.240922	0.814781	2.490919
	0.5								1.381568	0.744752	2.574004
	1.0								1.500127	0.684033	2.644810
1	0.5	0.0	1	0.2	0.2	0.5	0.5	0.5	1.240922	0.814781	2.490919
		0.5							1.381568	0.744752	2.574004
		1.0							1.500127	0.684033	2.644810
1	0.5	0.3	1.0	0.2	0.2	0.5	0.5	0.5	1.500127	0.443237	2.882918
			2.0						1.500127	0.610223	2.720084
			3.0						1.500127	0.684033	2.644810
1	0.5	0.3	1	0.1	0.2	0.5	0.5	0.5	1.500123	0.683236	0.683236
				0.3					1.500123	0.707381	2.617194
				0.5					1.500123	0.710888	2.615279
1	0.5	0.3	1.0	0.2	0.2	0.5	0.5	0.5	1.500123	1.463439	-3.185740
					0.6				1.500123	1.036418	1.735500
					1.0				1.500127	0.684033	2.644810
1	0.5	0.3	1.0	0.2	0.2	0.0	0.5	0.5	1.500127	1.189236	3.116440
						0.5			1.500127	0.913941	2.763214
						1.0			1.500127	0.684033	2.644810
1	0.5	0.3	1.0	0.2	0.2	0.5	0.0	0.5	1.500127	1.361740	1.957474
							0.5		1.500127	1.026602	2.297387
							1.0		1.500127	0.684033	2.644810
1	0.5	0.3	1.0	0.2	0.2	0.5	0.5	0.0	1.500127	0.780557	1.861002
								0.5	1.500127	0.723561	2.301518
								1.0	1.500127	0.684033	2.644810

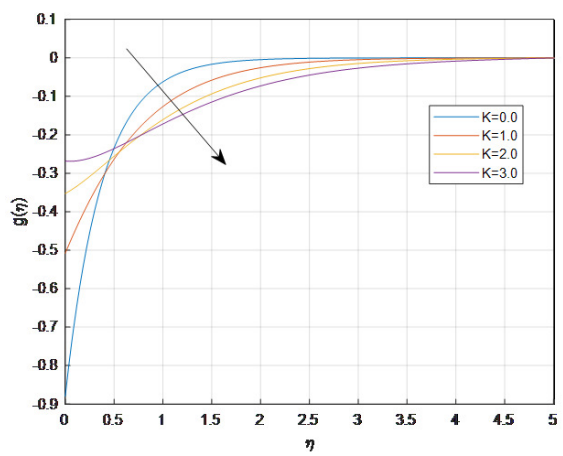

Figure 3: Change in microrotation g with varying K

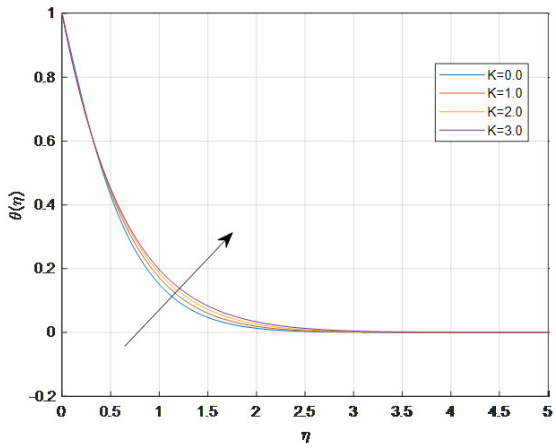

Figure 4: Change in temperature profile θ with varying K

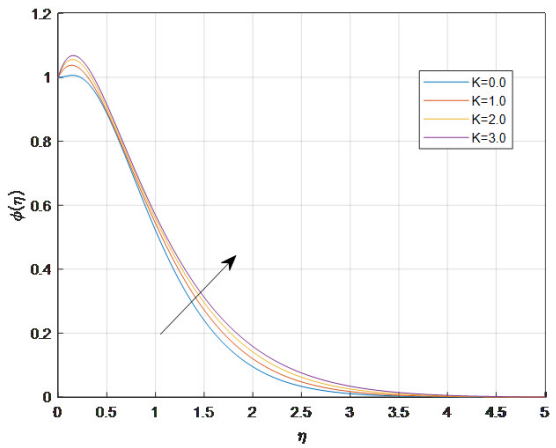

Figure 5: Change in concentration profile ϕ with varying K

The effect of Suction parameter is discussed in Figures 6-9. Suction enhances the axial velocity $f'(\eta)$ near the wall due to the removal of low-momentum fluid particles. This also accelerates the rotational motion of the fluid particles, leading to a steeper decay in $g(\eta)$ near the wall and then increases far away which is observed from Figure 6 and Figure 7. The temperature $\theta(\eta)$ and concentration $\phi(\eta)$ profiles both decrease with increasing suction in Figure 8 and Figure 9. This is expected, as suction reduces the fluid residence time near the wall, thereby enhancing both heat and mass transfer rates. Consequently, the thermal and solutal boundary layers become thinner with stronger suction effects.

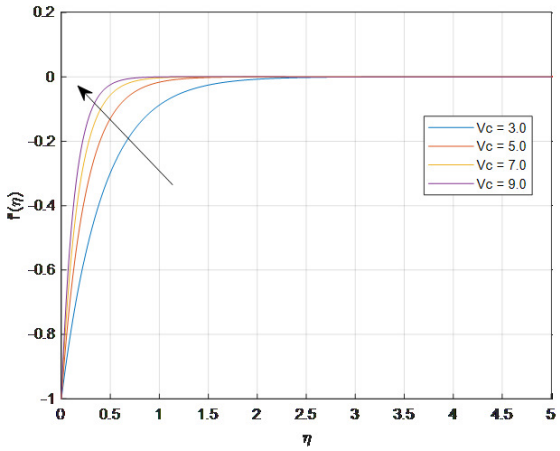

Figure 6: Change in velocity profile f' with varying Vc

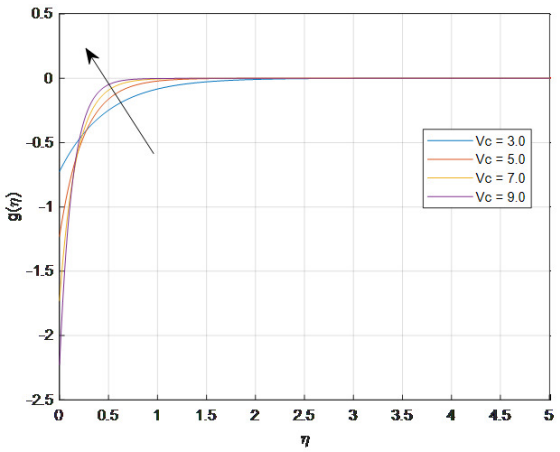

Figure 7: Change in microrotation g with varying Vc

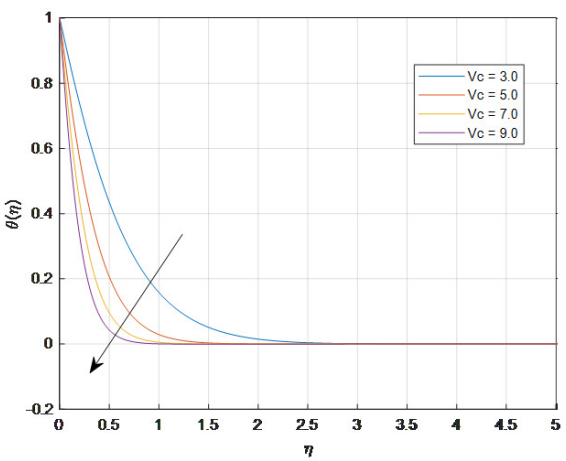

Figure 8: Change in temperature profile θ with varying Vc

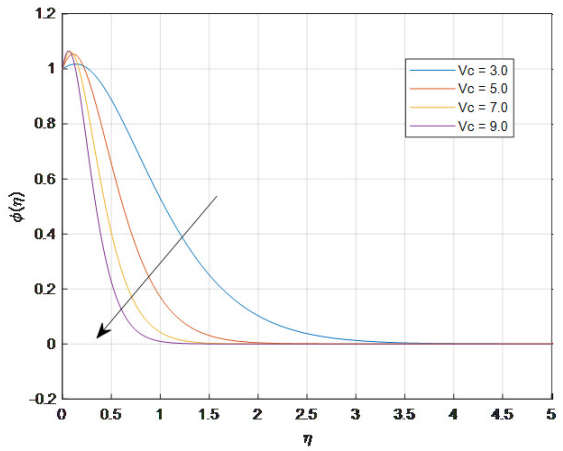

Figure 9: Change in concentration profile ϕ with varying Vc

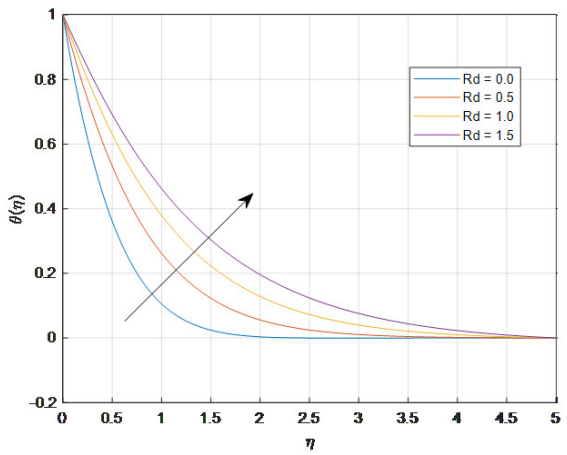

Figure 10: Change in temperature profile θ with varying Rd

Thermal radiation plays a vital role in high-temperature environments. Increasing the Radiation parameter Rd results in a significant increase in $\theta(\eta)$ in Figure 10, indicating that radiative heat enhances energy transport within the boundary layer. Thus, the thermal boundary layer becomes thicker.

The Thermophoresis parameter Nt accounts for the migration of nanoparticles due to temperature gradients. As Nt increases, the temperature profile $\theta(\eta)$ increases slightly in Figure 11 because more thermal energy is retained within the boundary layer due to enhanced particle movement from hot to cold regions. Meanwhile, the concentration profile $\phi(\eta)$ also increases noticeably with Nt as shown in Figure 12, as thermophoresis tends to push nanoparticles away from the heated surface, enriching the fluid bulk with particles. This broadens the concentration boundary layer, resulting in a thicker solutal field.

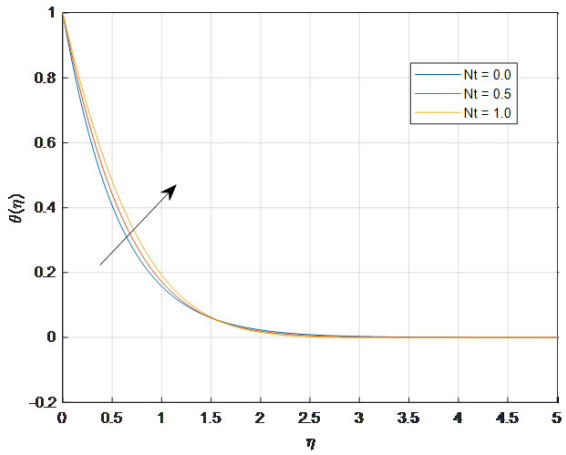

Figure 11: Change in temperature profile θ with varying Nt

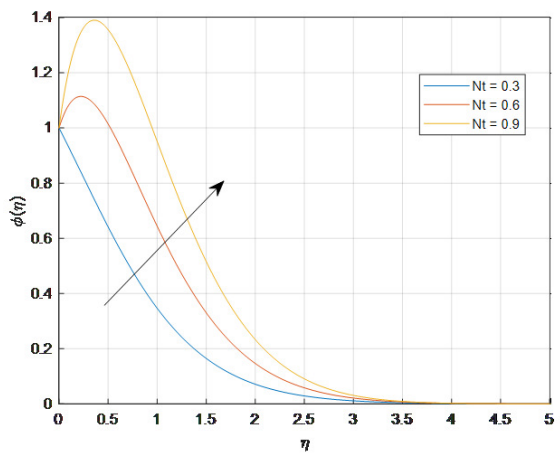

Figure 12: Change in concentration profile ϕ with varying Nt

The influence of Brownian motion parameter is exhibited in Figure 13-14. The Brownian motion parameter Nb models the random motion of nanoparticles. For the temperature profile $\theta(\eta)$ a rise in Nb generally causes an increase due to energy interactions between fluid molecules and nanoparticles. For the concentration profile $\phi(\eta)$, the effect is more pronounced. Higher Nb leads to reduced concentration near the surface and a thicker solutal boundary layer overall, as nanoparticles move more freely throughout the domain.

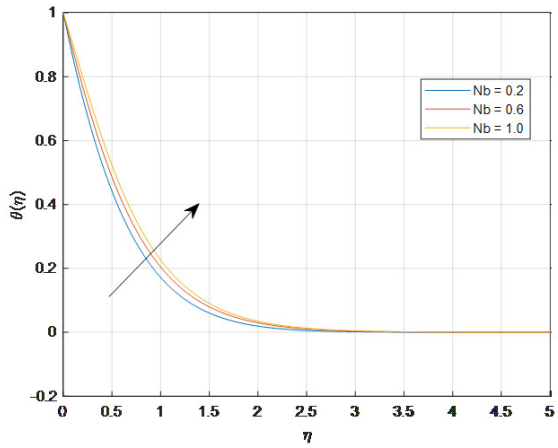

Figure 13: Change in temperature profile θ with varying Nb

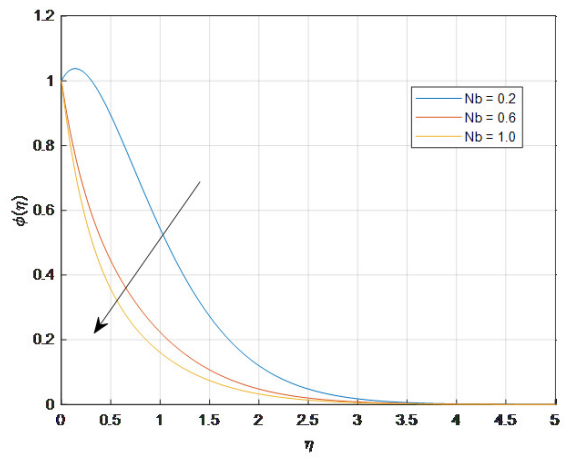

Figure 14: Change in concentration profile ϕ with varying Nb

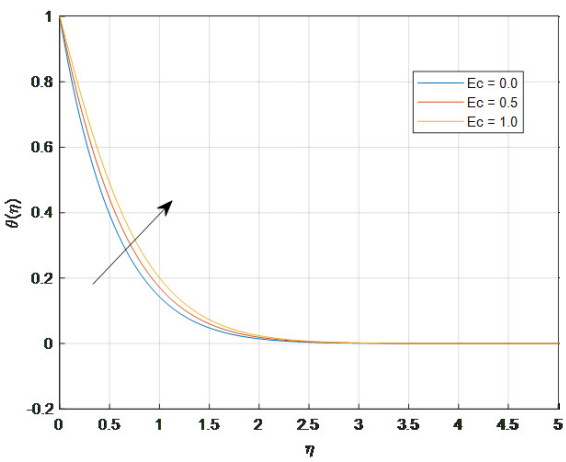

Figure 15: Change in temperature profile θ with varying Ec

The Eckert number signifies the effect of viscous dissipation. As Ec grows, the temperature profile $\theta(\eta)$ in Figure 15 shows a significant rise, particularly near the surface. This indicates that frictional heating due to velocity gradients contributes significantly to thermal energy, thereby thickening the thermal boundary layer. Interestingly, the concentration profile $\phi(\eta)$ in Figure 16 increases slightly with Ec, as elevated temperature gradients due to dissipation may reduce mass diffusivity indirectly.

Thermal diffusivity divided by momentum diffusivity is represented by the Prandtl number Pr. In Figure 17, a rise in Pr causes the temperature profile $\theta(\eta)$ to fall. Physically, this means that fluids with higher Pr have lower thermal diffusivity, allowing less heat to penetrate through the fluid, which results in a thinner thermal boundary layer.

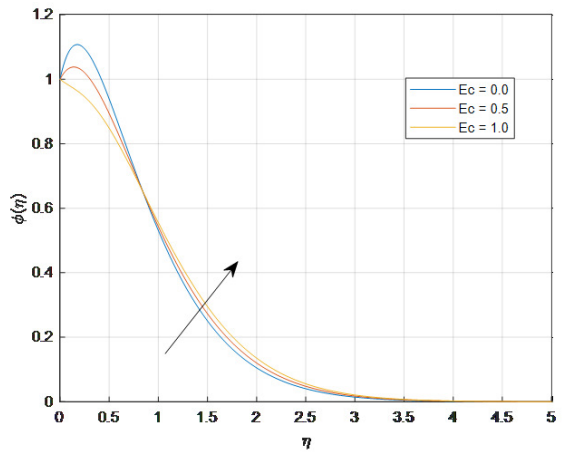

Figure 16: Change in concentration profile ϕ with varying Ec

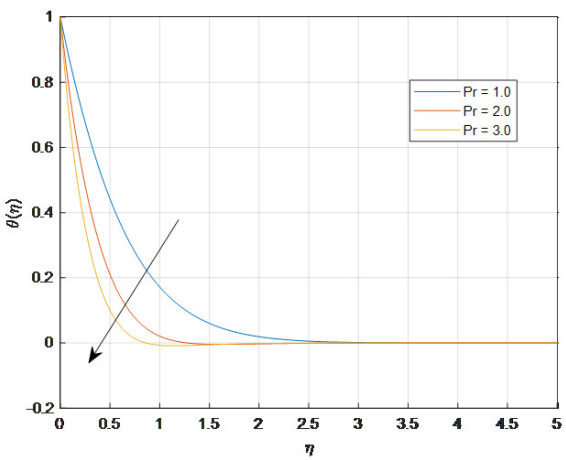

Figure 17: Change in temperature profile θ with varying Pr

The effect of chemical reaction parameter on temperature and concentration profiles is shown in Figure 18-19. The temperature profile increases with increase of chemical reaction from Figure 18. The chemical reaction parameter γ strongly influences the concentration profile $\phi(\eta)$. As γ increases, $\phi(\eta)$ decreases notably in Figure 19, indicating the depletion of species concentration due to destructive chemical reactions. This leads to a thinner solutal boundary layer.

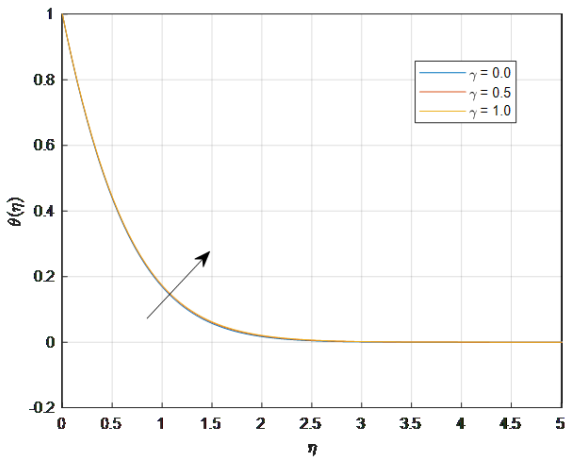

Figure 18: Change in temperature profile θ with varying γ

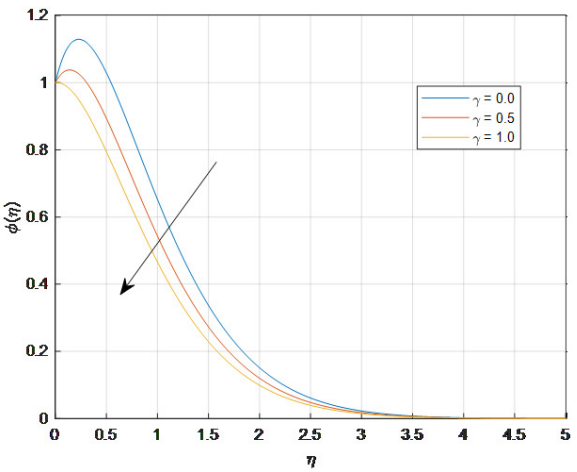

Figure 19: Change in concentration profile ϕ with varying γ

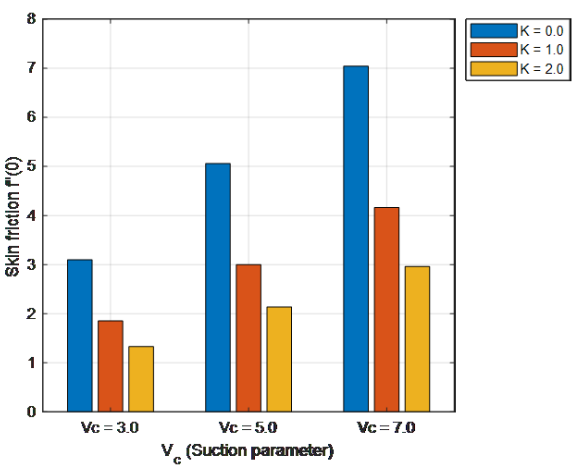

Figure 20: Change in Skin friction $f''(0)$ with varying Vc and K

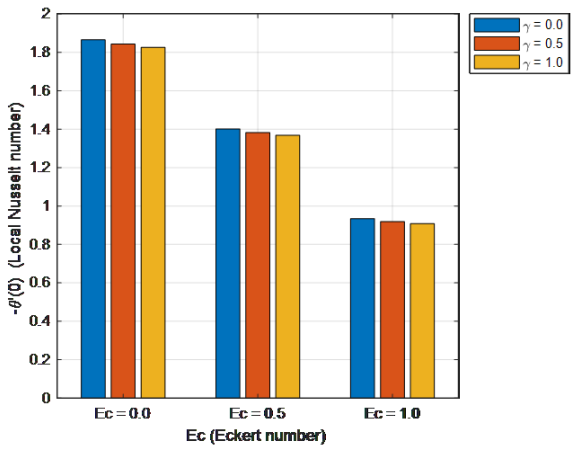

Figure 21: Change in local Nusselt number $-\theta'(0)$ with varying Ec and γ

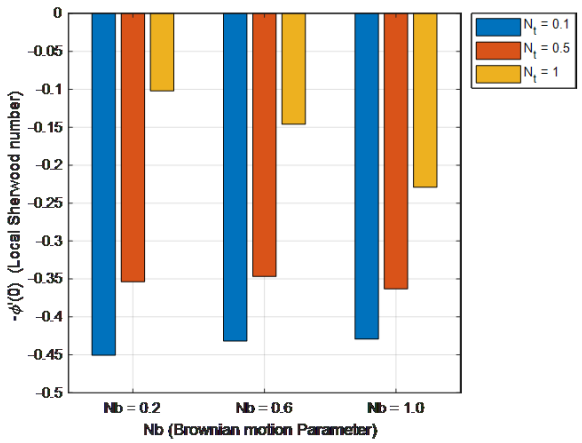

Figure 22: Change in local Sherwood number $-\phi'(0)$ with varying Nb and Nt

The combined effect of Suction parameter and Micropolar fluid parameter on Skin friction is depicted in Figure 20. At fixed Vc, increasing K reduces the skin friction. This confirms that micro rotation absorbs part of the shear energy, reducing wall shear stress. As Vc is increased, at each K, increasing Vc increases Skin friction. Suction compresses the boundary layer, increasing shear gradients at the wall. From Figure 21, it is understood that the local Nusselt number decreases with both increasing viscous dissipation and chemical reaction. Finally, the combined implications of Nb and Nt on local Sherwood number is discussed in Figure 22. Increasing Nb and Nb simultaneously leads to a reduction in mass transfer rate due to weakened concentration gradients caused by intensified nano particle diffusion and thermophoretic effect.

5. Conclusions

This paper gives a complete numerical evaluation of the steady magnetized micropolar nanofluid flow across a porous stretched sheet, considering the effects of viscous dissipation and chemical reaction. The impacts of important physical factors on velocity, microrotation, temperature and concentration profiles, as well as engineering quantities skin friction coefficient, local Nusselt number and local Sherwood number were comprehensively investigated. The following are the main results.

1. The suction parameter Vc increased the axial velocity near the surface and reduced both temperature and concentration profiles due to boundary layer thinning and shortened fluid residence

time.

2. The micropolar fluid parameter K reduced the axial velocity $f'(\eta)$ due to the energy absorbed by microrotation, while it enhanced $g(\eta)$, signifying stronger rotational effects.

3. Viscous dissipation Ec markedly raised $\theta(\eta)$ due to frictional heating, and slightly increased $\phi(\eta)$ potentially due to the indirect impact on diffusion coefficients.

4. The chemical reaction parameter γ increased the temperature field but caused a sharp decrease in the concentration profile $\phi(\eta)$, reflecting species depletion due to destructive reactions.

5. The Prandtl number Pr showed a cooling effect. As it increased, $\theta(\eta)$ dropped, indicating that fluids with lower thermal diffusivity maintain thinner thermal boundary layers.

6. Skin friction was found to decrease with increasing micropolar parameter K and increase with suction Vc, confirming that rotational microstructures reduce shear stress while suction sharpens shear gradients.

7. The local Nusselt number diminished with higher values of both Ec and γ, due to enhanced thermal resistance and reaction-induced energy absorption.

8. The local Sherwood number was adversely affected by simultaneous increases in Nt and γ, as thermophoresis and chemical reactions weaken the solutal gradient near the wall, reducing mass transfer rates.

The results provide valuable insights into the coupled heat and mass transfer mechanisms in micropolar nanofluids under complex physical effects, with potential applications in advanced cooling systems, chemical processing, and porous media engineering.

Acknowledgement

We acknowledge the reviewer's valuable time spent reading and providing feedback on this article. Your insightful comments and suggestions that might improve the standard of this paper are much appreciated. This study is not supported by any grants.

Nomenclature

u, v velocities along x and y directions(m/s)	γ Chemical reaction parameter
ρ Density (kg/m^3)	C_s Concentration susceptibility
ϑ Dynamic viscosity (kg/m s)	C_p Specific heat (J/kg. K)
σ Electric intensity	C Nanofluid concentration
k Micropolar fluid coefficient	m Boundary parameter
K Micropolar fluid parameter	M Magnetic number
φ_1 Porous medium	$\in$ Porosity parameter
B_0 Magnetic field strength	Rd Radiation parameter
N Microrotation velocity	D_f Dufour number
T Temperature (K)	Nb Brownian parameter
σ^* Stefen Boltzmann constant	Nt Thermophoresis parameter
τ_w Ratio of heating capacitance	Sc Schmidt number
D_B Brownian diffusion	V_c Suction parameter
D_T Thermophoresis diffusion	Ec Eckert number
k^* Mean absorption coefficient	η similarity variable

References

1. Eringen, A. C., *Theory of micropolar fluids*, J. Math. Mech. 16(1), 1–18, (1966).
2. Choi, S. U. S. and Eastman, J. A., *Enhancing thermal conductivity of fluids with nanoparticles*, Proc. ASME Int. Mech. Eng. Congr. Expo. 231, 99–105, (1995).
3. Buongiorno, J., *Convective transport in nanofluids*, J. Heat Transfer 128(3), 240–250, (2006).
4. Muhaimin, Kandasamy, R. and Hashim, I., *Effect of chemical reaction, heat and mass transfer on nonlinear boundary layer past a porous shrinking sheet in the presence of suction*, Nucl. Eng. Des. 240(5), 933–939, (2010).
5. Shateyi, S., *Thermal radiation and buoyancy effects on heat and mass transfer over a semi-infinite stretching surface with suction and blowing*, J. Appl. Math., Article ID 414830, (2008).
6. Khan, W. A. and Pop, I., *Boundary-layer flow of a nanofluid past a stretching sheet*, Int. J. Heat Mass Transfer 53(11–12), 2477–2483, (2010).
7. Narender, G., Govardhan, K. and Sreedhar Sarma, G., *MHD casson nanofluid past a stretching sheet with the effects of viscous dissipation, chemical reaction and heat source/sink*, J. Appl. Comput. Mech. 4, 2040–2048, (2021).
8. Govardhan, K., Narender, G. and Sreedhar Sarma, G., *Viscous dissipation and chemical reaction effects on MHD casson nanofluid over a stretching sheet*, Malays. J. Fundam. Appl. Sci. 15(4), 585–592, (2019).
9. Ishak, A., Nazar, R. and Pop, I., *Heat transfer over a stretching surface with variable heat flux in micropolar fluids*, Phys. Lett. A 372(5), 559–561, (2009).
10. Srinivasacharya, D. and Jagadeeshwar, P., *Effect of variable viscosity, thermal conductivity, and hall currents on the flow over an exponentially stretching sheet with heat generation/absorption*, Int. J. Energy Clean Environ. 19(1–2), 67–83, (2018).
11. Bég, O. A., Zueco, J. and Chang, T. B., *Numerical analysis of hydromagnetic gravity-driven thin film micropolar flow along an inclined plane*, Chem. Eng. Commun. 198(3), 312–331, (2011).
12. Ajala, O. A. and Adegbite, P., *Hydromagnetic flow of micropolar nanofluids with co-effects of thermal radiation and chemical reaction over an inclined permeable stretching surface*, Beni-Suef Univ. J. Basic Appl. Sci. 12, 86, (2023).
13. Sachhin, S. M., Ankitha, P. K., Sachin, G. M., Mahabaleshwar, U. S., Shevchuk, I. V., Nayakar, S. N. R. and Kadli, R., *Chemically reactive micropolar hybrid nanofluid flow over a porous surface in the presence of an inclined magnetic field and radiation with entropy generation*, Physics 6, 1315–1344, (2024).
14. Sulochana, C. and Mahalaxmi, B., *Thermophoresis and brownian motion effects on williamson nanofluid flow past a stretching surface with thermal radiation and chemical reaction*, Heat Transfer 51(3), 2761–2779, (2022).
15. Sreedhar Sarma, G., Subbaiah, G. V., Reddy, D. S., Manjula, N. and Umakanth, M., *Predictor corrector approach on 3D casson nanofluid flow over rotating frame with prescribed heat flux and viscous heating under the influence of radiation*, J. Adv. Res. Fluid Mech. Therm. Sci. 130(2), 228–244, (2025).
16. Khan, U., Zaib, A., Ishak, A., Godhbani, R. and Elkamchouchi, D. H., *Insight into the hydrothermal performance for buoyancy flow of a micropolar nanofluid past a stretching/shrinking sheet with viscous dissipation effects*, J. Therm. Anal. Calorim. 150, 8043–8058, (2025).
17. Panda, S., Baithalu, R., Baag, S. and Mishra, S. R., *Behaviour of effective heat transfer rate in radiating micropolar nanofluid over an expanding sheet with slip effects*, Partial Differ. Equ. Appl. Math. 11, 100851, (2024).
18. Alqahtani, A. M., Ullah, B., Ahmad, B., Khan, U., Wahab, H. A. and Alroobaea, R., *Thermal analysis of micropolar hybrid nanofluid inspired by 3d stretchable surface in porous media*, Nanoscale Adv. 5, 6216–6227, (2023).
19. Zegeye, G. B., Haile, E. and Awgichew, G., *Viscous dissipation and joule heating effects of carreau nanofluid axisymmetric flow past unsteady radially stretching porous disk*, Int. J. Thermofluids 22, 100655, (2024).
20. Hayat, T., Mustafa, M. and Pop, I., *Heat and mass transfer for soret and dufour effects on mixed convection boundary layer flow over a stretching vertical surface in a porous medium filled with a viscoelastic fluid*, Commun. Nonlinear Sci. Numer. Simul. 15(5), 1183–1196, (2010).
21. Rehman, A., Khan, D., Mahariq, I., Elkotb, M. A. and Elnaqeeb, T., *Viscous dissipation effects on time-dependent MHD casson nanofluid over stretching surface: a hybrid nanofluid study*, J. Mol. Liq. 408, (2024).
22. Ghosh, S. and Mukhopadhyay, S., *Unsteady MHD three-dimensional flow of nanofluid over a stretching surface with zero nanoparticles flux and thermal radiation*, Waves Random Complex Media 34(4), 2637–2653, (2021).
23. Sarma, G. S., Narender, G. and Govardhan, K., *Comprehensive study of buongiorno nanofluid model for MHD casson flow on an inclined porous stretching surface with heat source/sink and viscous dissipation*, Z. Angew. Math. Mech. 104, (2024).
24. Muhammad, F., Majeed, A., Ijaz, N., Barghout, K. and Abu-Libdeh, N., *Exploration of heat transfer rate and chemically reactive bio-convection flow of micropolar nanofluid with gyrotactic microorganisms*, BioNanoSci. 14, 1141–1156, (2024).
25. Abbas, T., Khan, S. U., Saeed, M., Abu El Maati, L. and Khan, M. I., *Feasibility and angular velocity analysis of micropolar nanofluid suction effects*, Alexandria Eng. J. 124, 38–45, (2025).

26. Abdelgaber, K. M., Fathy, M. and Abbassi, P. K., *Heat and mass transfer of micropolar fluid flow over a stretching sheet by legendre collocation method*, Sci. Rep. 15, 25921, (2025).

27. Pudhari, S., Hassan, A. M., Goud, B. S. and Ranjit Kumar, E., *Mathematical study of MHD micropolar fluid flow with radiation and dissipative impacts over a permeable stretching sheet: slip effects phenomena*, Front. Heat Mass Transfer 21(1), 539–562, (2023).

28. Zigta, B., *Thermal radiation, chemical reaction and viscous dissipation effects on MHD mixed convection flow of micropolar fluid with stretching surface*, J. Fluid Dyn. 3(2), 45–64, (2022).

29. Adeyemi, C. A., Olajuwon, B. I., Bayo, J. A. and Raji, M., *Dynamics of thermal radiation and heat generation/absorption on a viscous MHD micropolar fluid over a stretching sheet with suction/injection*, J. Therm. Eng. 10(4), 836–846, (2024).

30. Meenakshi, V., Renuka, S., Sreehari, P., Misra, S. and Sreedhar Sarma, G., *Impact of chemical reaction on three-dimensional casson nanofluid flow over a rotating surface with prescribed heat flux, viscous dissipation, and heat source/sink effects*, Bol. Soc. Paran. Mat. 43, 1–19, (2025).

31. Ahmed, B. and Al-Radaideh, A., *Examining heat and mass transfer in MHD williamson micropolar fluid flow on a stretching sheet with viscous dissipation, chemical reaction, and nonlinear heat generation/absorption*, J. Adv. Res. Numer. Heat Transfer 33(1), 30–47, (2025).

32. Shehzad, S. A., Reddy, M. G., Rauf, A., Mushtaq, T. and Abbasi, F. M., *Magnetohydrodynamic squeezing micropolar nanofluid flow confined in parallel disks with implication of maxwell–cattaneo law*, Phys. Scr. 98(6), 065201, (2023).

Sreedhar Sarma Gobburu,

Department of H&S(Mathematics),

CVR College of Engineering,

Hyderabad, Telangana, India.

E-mail address: sarma.sreedhar@gmail.com